A Robust Controller Based on High-Order Fully Actuated Approach for DC–DC Buck Converter With Constant Power Loads in DC Microgrids

Yadong Wei, *Student Member, IEEE*, and Bo Zhang, *Fellow, IEEE*

***Abstract*—The negative incremental impedance characteristics exhibited by constant power loads (CPLs) in dc microgrids introduce instability in upstream dc–dc buck converters. In this article, a robust control strategy based on high-order fully actuated system approach is proposed for globally stabilizing and regulating the buck converter feeding CPLs. First, a second-order fully actuated model incorporating nonlinear uncertainties from input, load and system parameters disturbances is derived to describe system dynamics. A robust control law is then synthesized from the perspective of second-order system dynamics by compensating for the negative effects introduced by CPLs and reconstructing the desired closed-loop dynamics through first-order state feedback. Second, an uncertainty boundary estimator is designed to enhance system robustness against disturbances without precise measurements of load or input. A simple differential state observer is adopted to avoid the use of noise-sensitive differentiators. The proposed controller not only ensures large signal stability of the system, but also achieves accurate tracking and fast dynamic response within a wide working range. Simulations and experiments are further conducted to validate the effectiveness and superiority of the presented controller.**

***Index Terms*—Constant power load (CPL), dc microgrids, dc–dc buck converter, high-order fully-actuated (HOFA) system approach, nonlinear uncertainties, robust control.**

I. Introduction

DISTRIBUTED renewable energy sources have recently gained significant attention and have been developing rapidly due to increasing environmental concerns and the depletion of nonrenewable resources [1]. The dc microgrids have become a popular application for integrating these distributed renewable energy sources, such as solar photovoltaics, wind turbines, and fuel cells, into conventional power systems by using power electronic converters as interfaces [2]. The general structure of a dc microgrid system is illustrated in Fig. 1. A

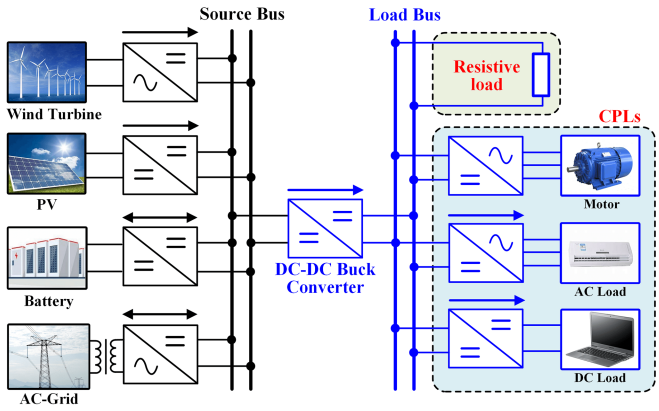

Fig. 1. Structure diagram of a DC microgrid system.

significant challenge for dc microgrids is the negative incremental impedance characteristic due to constant power loads (CPLs), which reduces system damping and leads to the limit cycle phenomenon with dc bus voltage oscillations [3]. This instability can destabilize the upstream converters and even the feeder system, posing serious risks to the safe and stable operation of the dc microgrid system [4], [5].

To address the stability issues posed by CPLs, many previous efforts have focused on passive damping methods [6], [7], which compensate for the negative incremental impedance effect by adding passive components such as inductors, capacitors, and resistors. Although these methods are simple to implement, they result in increased power dissipation. To avoid the inefficiency issue of passive damping methods, active damping methods have been presented in [8] and [9], which create the damping effect by modifying the control structure without altering the hardware configuration of the system. However, these methods can only compensate for a limited amount of CPL. Moreover, all of these methods are based on linearized small-signal models and frequency-domain design techniques, which can only guarantee system stability around operating points but not in situations where the system is subject to large disturbances.

In order to overcome the limitations of small-signal based approaches, numerous more effective nonlinear control techniques have been proposed for stabilizing CPLs in large-signal sense, including the passivity-based control (PBC) [10], [11], [12], sliding mode control (SMC) [13], [14], feedback

Received 13 October 2024; revised 20 December 2024 and 17 January 2025; accepted 18 February 2025. Date of publication 24 February 2025; date of current version 14 April 2025. This work was supported by the National Natural Science Foundation of China under Grant U2166601. Recommended for publication by Associate Editor X. Ruan. *(Corresponding author: Bo Zhang.)*

The authors are with the School of Electric Power, South China University of Technology, Guangzhou 510640, China (e-mail: 202210182639@mail.scut.edu.cn; epbzhang@scut.edu.cn).

Color versions of one or more figures in this article are available at https://doi.org/10.1109/TPEL.2025.3544683.

Digital Object Identifier 10.1109/TPEL.2025.3544683

linearization method [15], [16], backstepping method [17], [18], model predictive control (MPC) [19], [20], energy shaping control (ESC) [21], and generalized dynamic predictive control (GDPC) [22].

In [10], an adaptive PBC was proposed to damp negative effects caused by CPLs by shaping the dissipation function. A nonlinear disturbance observer (NDO) is incorporated to estimate the system disturbances online and feed them forward to the PBC, thereby enhancing the robustness of the controller. However, there is a tradeoff between tracking speed and accuracy in the observer, which makes it hard to ensure optimal performance of both voltage tracking and transient responses. In [13], a discrete quasi-slide mode controller (DQSMC) was proposed to address the stability issues caused by CPLs, with a second-order sliding mode disturbance observer (S^2 MDO) embedded for enhancing the disturbance rejection and chattering suppression capability of the system. Although this fixed-frequency and discrete realization can mitigate the well-known chattering problem in conventional SMC, but the ideal sliding surface cannot be fully reached, leading to reduced dynamic performance and robustness. In [15], a feedback linearization method with a reduced-order power observer for feedforward compensation was developed to eliminate the nonlinearity and negative incremental impedance effects introduced by CPLs. However, this method requires an accurate model of the underlying physical system, the uncertainties and disturbances in the system parameters can deteriorate control performance. Moreover, the stability of the system in large-signal sense cannot be proved in the presence of parameter mismatch. In [19], an MPC controller employing a nonlinear inductor was presented to achieve faster dynamic response and an extended stability range. However, this approach requires an additional sensor to measure the input voltage, as well as hardware modification to the inductor and the increased online computational burden adds to the cost complexity of system implementation. In [35], a boundary controller was proposed that utilizes a first-order switching surface to control the buck converter with CPLs. This method eliminates the negative effects introduced by CPLs through a linear switching surface with a negative slope. While an appropriately chosen slope can optimize response time, the hysteresis-based design of the controller results in variable switching frequency and degraded ripple effect. In addition, the load information must be fed forward to the controller to adjust the vertical position of the switching surface, obtaining a satisfactory steady-state performance during significant CPL power variations.

Recently, the high-order fully actuated (HOFA) system approach has emerged as a promising method for system modeling and control design [23]. The core concept of this method involves using variable elimination to transform the origin physical model into a higher-order model satisfying full-actuation condition (i.e., HOFA model). The property of full-actuation allows for the removal of all original dynamics and enables the arbitrary assignment of pole locations via state feedback control [24]. Consequently, the control law can be synthesized to achieve a desired closed-loop system in a straightforward and explicit way.

Compared to the first-order state space (FOSS) model, the HOFA system model provides a more natural representation of high-order dynamic systems. The coefficient matrices of the preserved high-order differential terms capture essential characteristics of the dynamic system, such as damping ratios and attenuation coefficients, which are advantageous for control system design [25]. Within the framework of HOFA system theory, notable progress has been achieved in addressing practical problems in air-bearing spacecrafts [26], flexible servo systems [24], quadrotor aircrafts [27], and dc microgrid systems [28].

Inspired by [29], this article proposes a novel robust control strategy based on HOFA system approach for stabilizing and regulating a dc–dc buck converter with CPLs in a dc microgrid. The contributions of this article are outlined as follows.

1) Unlike FOSS model-based methods in previous literature, the proposed method employs an uncertain fully-actuated model described by a second-order differential equation. This model preserves complete information of the original system's high-order dynamics, and the full actuation property of the model facilitates the design of controller to compensate for the negative effects of the CPL, which manifests as a negative component in the first-order differential dynamics of the output voltage.
2) A novel robust control strategy is proposed to stabilize buck converters with CPLs in dc microgrids, ensuring large-signal stability. The controller dynamically compensates for the CPL's variable negative damping effect based on output voltage and reconstructs desired closed-loop dynamics through first-order state feedback. By driving the output voltage's differential to exponential convergence to zero, it allows the inductor current to track its steady-state reference without needing additional sensors to detect load currents under varying load.
3) A differential state observer is adopted to obtain the differential information of the output voltage by detecting the output capacitor's current. This eliminates the need for noise-sensitive differentiators, thereby enhancing the control system's robustness against noise.
4) A novel uncertainty boundary estimator is proposed to estimate the upper bound of uncertainties, which is then fed forward to the proposed robust controller, guaranteeing the global asymptotic convergence and large-signal stability against disturbances, without requiring precise information about system parameters.
5) A systematic parameter design process is proposed for tuning control parameters based on the desired dynamic response of the closed-loop system, enabling optimal design of both transient and steady-state performance.

The rest of this article is organized as follows. Section II derives an uncertain HOFA model of the dc–dc buck converter feeding resistive load and CPL loads and proposes a HOFA-based robust controller to stabilize this system. Section III discusses the stability analysis of the control system. In Section IV, an uncertainty boundary estimator and a differential state observer are proposed, along with detailed parameter design rules for the controller. Section V presents the simulation

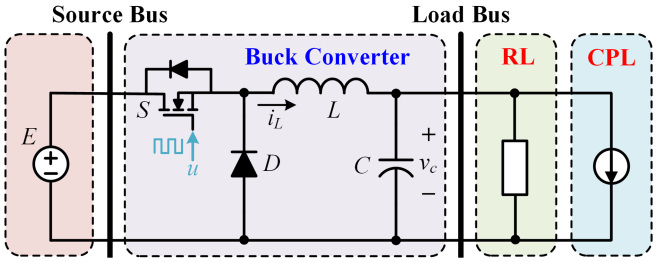

Fig. 2. Circuit schematic of buck converter feeding RL and CPL.

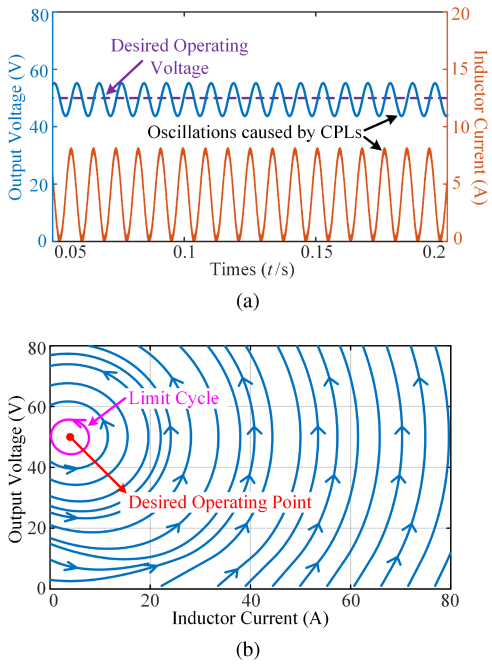

Fig. 3. Schematic representation of the effect of CPL on converter stability. (a) Voltage and current of buck converter under open-loop control. (b) Phase trajectory of buck converter under open-loop control.

verification and comparative analysis. The experimental results are subsequently provided in Section VI. Finally, Section VII concludes this article.

II. Uncertain HOFA Model and Robust Controller of Buck Converter

A. Problem Description

Fig. 2 shows the circuit schematic of a buck converter supplying a hybrid load comprising a resistive load (RL) and a CPL in parallel, where S, D, L, and C represent the switch, diode, inductor, and filter capacitor, respectively. E denotes the dc input voltage, i_L is the inductor current, and v_o is the output voltage equal to filter capacitor voltage v_c.

Due to the negative incremental impedance characteristic introduced by the CPL, the system state of the converter under open-loop control will converge to limit cycles rather than the desired operating point, as illustrated in Fig. 3(b). The output voltage and inductor current of the converter exhibit wide fluctuations, as depicted in Fig. 3(a), resulting in poor output power quality, increased current stress on devices, and potential instability of upstream converters.

To achieve global stability in the closed-loop system, the HOFA approach is utilized to model the system and compensate the nonlinearities introduced by the CPL through state-feedback control. To ensure robustness of the proposed controller, uncertainties are taken into account in the derivation of the HOFA model, and a robust tracking controller is devised based on this uncertain HOFA model.

B. Uncertain HOFA Model of Buck Converter

According to the operating principle of buck converter in continuous conduction mode, the dynamic model of buck converter described in averaged state model is given by

$$\begin{cases} L\frac{\mathrm{d}i_L}{\mathrm{d}t} = Ed - v_c \\ C\frac{\mathrm{d}v_c}{\mathrm{d}t} = i_L - \frac{v_c}{R} - \frac{P}{v_c} \end{cases} \tag{1}$$

where $d \in [0, 1]$ represents the duty cycle of the switch.

Defining the system state $\boldsymbol{x} \in \mathbb{R}^2$ as $\boldsymbol{x} = [x_1\ x_2]^T = [i_L\ v_c]^T$ and selecting the duty cycle d as the control input u, we consider system uncertainties stemming from input instability, load disturbance, and parameter tolerance of inductance and capacitance. The first-order state space model with nonlinear uncertainties can thus be expressed in the form of a first-order affine differential equation as

$$\dot{\boldsymbol{x}} = \boldsymbol{f}(\boldsymbol{x}, u) + \boldsymbol{b}u \tag{2}$$

$$\boldsymbol{f}(\boldsymbol{x}, u) = \begin{bmatrix} -\frac{x_2}{L_o} + \Delta f_1(x_2, u) \\ \frac{x_1}{C_o} - \frac{x_2}{C_o R_o} - \frac{P_o}{C_o x_2} + \Delta f_2(x_1, x_2) \end{bmatrix}, \boldsymbol{b} = \begin{bmatrix} \frac{E_o}{L_o} \\ 0 \end{bmatrix} \tag{3}$$

where E_o, L_o, C_o, R_o, and P_o represent the known nominal values of corresponding system parameters, and the nonlinear uncertainty terms $\Delta f_1(x_2, u)$ and $\Delta f_2(x_1, x_2)$ are represented as

$$\Delta f_1(x_2, u) = \left(\frac{1}{L_o} - \frac{1}{L}\right) x_2 + \left(\frac{E}{L} - \frac{E_o}{L_o}\right) u \tag{4}$$

$$\Delta f_2(x_1, x_2) = \left(\frac{1}{C} - \frac{1}{C_o}\right) x_1 + \left(\frac{1}{C_o R_o} - \frac{1}{CR}\right) x_2 + \left(\frac{P_o}{C_o} - \frac{P}{C}\right) \frac{1}{x_2}. \tag{5}$$

According to the HOFA system theory [23], the system model represented by (2) is under-actuated, as the dimension of the control input u is smaller than the dimension of the system state $\boldsymbol{x}$. Consequently, the control matrix $\boldsymbol{b}$ is not invertible, rendering the input u incapable of decouplingly controlling the first-order dynamics of all system states. Therefore, the HOFA approach is employed to transform the uncontrollable system state into the internal dynamics of a higher-order fully actuated system.

In this model, without the need for a coordinate transformation, the following equation in the pseudostrict-feedback form

can be obtained:

$$\begin{cases} \dot{x}_2 = \frac{x_1}{C_o} - \frac{x_2}{C_o R_o} - \frac{P_o}{C_o x_2} + \Delta f_2(x_1, x_2) \\ \dot{x}_1 = -\frac{x_2}{L_o} + \Delta f_1(x_2, u) + \frac{E_o}{L_o} u. \end{cases} \tag{6}$$

Taking differentials of the first equation in (6), yields

$$\ddot{x}_2 = \frac{\dot{x}_1}{C_o} - \frac{\dot{x}_2}{C_o R_o} + \frac{P_o}{C_o x_2^2} \dot{x}_2 + \Delta \dot{f}_2(x_1, x_2). \tag{7}$$

Introducing the first equation of (6) into (7), the second-order fully actuated model with uncertainties of buck converter can be derived as

$$\ddot{x}_2 = f(x_2, \dot{x}_2) + \Delta f(x_2, \dot{x}_2) + Bu \tag{8}$$

$$f(x_2, \dot{x}_2) = -\frac{1}{L_o C_o} x_2 - \left(\frac{1}{R_o C_o} - \frac{P_o}{C_o x_2^2} \right) \dot{x}_2 \tag{9}$$

$$\Delta f(x_2, \dot{x}_2) = \frac{1}{C_o} \Delta f_1(x_2, u) + \Delta \dot{f}_2(x_1, x_2) \tag{10}$$

where $\Delta f(x_2, \dot{x}_2)$ represents the nonlinear uncertainty term in the second-order dynamics of the output voltage x_2, and $B = E_o/(L_o C_o)$, which satisfies the fully actuated condition

$$\det(B) \neq 0, \forall x_2^{(i)} \in \mathbb{R}, i = 0, 1. \tag{11}$$

For the fully actuated system model (8), the state x_2 (i.e., output voltage of the converter) is fully controllable. This enables the attainment of closed-loop systems with arbitrary characteristics through the design of control law u.

C. Analysis of the Negative Effect Caused by CPL

Consider the fully-actuated system model of the converter without the nonlinear uncertainty term $\Delta f(x_2, \dot{x}_2)$, expressed as a standard second-order system equation

$$\ddot{x}_2 + \left(\frac{1}{RC} - \frac{P}{C x_2^2} \right) \dot{x}_2 + \frac{1}{LC} x_2 = Bu \tag{12}$$

where the term $[1/(RC) - P/(Cx_2^2)]\dot{x}_2$ which associated with the rate of change $\dot{x}_2$ of the system output, functions as the system damping term. It determines the system's dissipation and attenuation characteristics, influencing how the system responds to disturbances. The nonlinear damping coefficient $c(x_2) = 1/(RC) - P/(Cx_2^2)$ indicates that the CPL provides a variable damping effect to the system that changes as the output voltage varies.

The negative incremental impedance effect caused by the CPL manifests as a negative component in the damping term, indicating a reduction in system damping. Conversely, the passive impedance effect of the resistive load appears as a positive component in the damping term, signifying an increase in system damping. When $R > P/(x_2^*)^2$, the resistive load dominates, it has $c(x_2^*) > 0$, the system energy is dissipative at the equilibrium point $x_2 = x_2^*$, allowing the positive damping force to decay the amplitude of the oscillation. The system can be asymptotically stabilised at arbitrary equilibrium point $x_2^* \in [0, E]$ even under an open-loop control $u = x_2^*/E$. Conversely, when $R \leq P/(x_2^*)^2$, the CPL dominates, resulting in $c(x_2^*) < 0$. Here, the system energy becomes nondissipative at the equilibrium point, and the negative damping force drives the amplitude of the oscillations to increase, the system is unstable at the equilibrium point, leading to the limit cycle phenomenon with dc bus voltage oscillations under the open-loop control, as shown in Fig. 3.

To address the instability introduced by the constant power load in the dc microgrids, where CPL dominate, the core idea of the proposed method is to compensate for the negative component in the open-loop first-order differential dynamics of the output voltage through state feedback. The fully-actuated system model, characterized by an invertible control matrix, facilitates the design of a state-feedback control law, providing a favorable framework for resolving the instability issues associated with CPLs from the perspective of higher-order system dynamics. In addition, unlike most existing methods that only tackle the negative damping effect caused by CPL at the equilibrium point, the proposed method dynamically compensates for the variable negative damping effect of CPL, which varies with output voltage, thereby ensuring large-signal stability under varying voltage reference conditions.

Considering the uncertainty term $\Delta f(x_2, \dot{x}_2)$ in the fully actuated model as given in (8), the constant power load P is divided into two components: 1) the normal value P_o; and 2) the disturbance term $\Delta P = P - P_o$, which is incorporated into the nonlinear uncertainty term. The determined portion of the negative incremental impedance effect caused by the CPL can be directly offset by state feedback, while the uncertain portion is estimated and dynamically compensated for in the proposed controller, thereby ensuring the system's stability in the Lyapunov sense.

D. Proposed Robust Controller

To achieve accurate tracking and fast dynamic response of the output voltage, consider the following desired liner closed-loop system:

$$\ddot{e} + A_1 \dot{e} + A_0 e = 0 \tag{13}$$

where $e = x_2 - x_2^*$ is the tracking error between the output voltage x_2 and its reference value x_2^*. A_1 and A_0 are the coefficients of the closed-loop system. According to *Routh–Hurwitz criterion*, when the coefficients satisfy the conditions $A_1 > 0$ and $A_0 > 0$, the closed-loop system is stable, and the tracking error e converges globally and asymptotically to 0.

Since the desired output voltage of the buck converter is dc, x_2^* is a constant value, and thus $\ddot{x}_2^* = \dot{x}_2^* = 0$. Therefore, the equation of the desired closed-loop system (13) can be rewritten as

$$\ddot{x}_2 + A_1 \dot{x}_2 + A_0 (x_2 - x_2^*) = 0. \tag{14}$$

Because that the control matrix B is invertible, by combining (8) and (14), the desired closed system (13) can be achieved by applying the following ideal controller:

$$\begin{cases} u = u_c + u_f \\ u_c = -B^{-1} \left(f(x_2, \dot{x}_2) + \Delta f(x_2, \dot{x}_2) \right) \\ u_f = -B^{-1} (A_1 \dot{x}_2 + A_0 x_2 - A_0 x_2^*). \end{cases} \tag{15}$$

The controller comprises two components, where the first term u_c is designed to offset all open-loop nonlinear dynamics, including the negative incremental impedance effect introduced by

the CPL, thereby achieving linearization, while the second term u_f is employed to reconstruct the desired closed-loop system.

However, the uncertain term $\Delta f(x_2, \dot{x}_2)$ is caused by disturbances and tolerances in system parameters, which cannot be measured accurately. Therefore, the term u_c in the ideal controller is difficult to achieve. Inspired by Theorem 3.4 in [29], if the uncertainty term satisfies the boundary condition

$$\|\Delta f(x_2, \dot{x}_2)\| \leq \rho(x_2, \dot{x}_2) \tag{16}$$

where $\rho(x_2, \dot{x}_2)$ is a nonnegative continuous scalar function representing the absolute boundary of the uncertainty term $\Delta f(x_2, \dot{x}_2)$. Then, the compensatory term u_c in (15) can be revised as

$$u_c = -B^{-1}\left(f(x_2, \dot{x}_2) + \frac{\rho^2(x_2, \dot{x}_2)}{4\varepsilon} C_o^2 L_o \dot{x}_2\right) \tag{17}$$

to dynamically and partially compensate for the nonlinearities in the open-loop system, thereby obtaining the following approximate linear closed-loop system:

$$\ddot{e} + A_1\dot{e} + A_0 e = -\frac{\rho^2(x_2, \dot{x}_2)}{4\varepsilon} C_o^2 L_o \dot{x}_2 + \Delta f(x_2, \dot{x}_2) \tag{18}$$

where the states of the system converge globally asymptotically to a sufficiently small neighbourhood near the equilibrium point

$$\Omega = \left\{(x_2, \dot{x}_2) \left| \frac{1}{2} C_o (x_2 - x_2^*)^2 + \frac{1}{2} C_o^2 L_o (\dot{x}_2)^2 \leq \frac{\varepsilon}{\mu} \right.\right\}. \tag{19}$$

Here, ε and μ are positive numbers that satisfy

$$\mathrm{Re}\lambda_i \left(\begin{bmatrix} 0 & 1 \\ -A_0 & -A_1 \end{bmatrix} \right) < -\frac{\mu}{2}, i = 1, 2. \tag{20}$$

Combining (15) and (17), the proposed robust controller can be expressed as

$$\begin{aligned} u = & -\frac{L_o C_o}{E_o}\left(-\frac{1}{L_o C_o} x_2 - \left(\frac{1}{R_o C_o} - \frac{P_o}{C_o x_2^2}\right)\dot{x}_2 \right. \\ & \left. + \frac{\rho^2(x_2, \dot{x}_2)}{4\varepsilon} C_o^2 L_o \dot{x}_2 + A_0 x_2 + A_1 \dot{x}_2 - A_0 x_2^*\right) \end{aligned} \tag{21}$$

where the term $-B^{-1}P_o\dot{x}_2/(C_o x_2^2)$ offsets the determined portion of the negative incremental impedance effect caused by the CPL, while the term $-B^{-1}\rho^2 C_o^2 L_o \dot{x}_2/(4\varepsilon)$ estimates and dynamically compensates for the uncertain portion, thereby ensuring the system's stability in the Lyapunov sense.

III. Stability Analysis of Closed-Loop System

The stability of the closed-loop system is demonstrated in this section using the Lyapunov stability theory.

After substituting the proposed robust control law (21) into the open-loop system (8), the dynamic equation of the closed-loop system can be expressed as (18). Let $\boldsymbol{z} = [e\ \dot{e}]^T$, and

$$\boldsymbol{A}_c = \begin{bmatrix} 0 & 1 \\ -A_0 & -A_1 \end{bmatrix} \tag{22}$$

$$\xi(x_2, \dot{x}_2) = -\frac{\rho^2(x_2, \dot{x}_2)}{4\varepsilon} C_o^2 L_o \dot{x}_2 + \Delta f(x_2, \dot{x}_2). \tag{23}$$

Then, equation of the closed-loop system can be rewritten as

$$\dot{\boldsymbol{z}} = \boldsymbol{A}_c \boldsymbol{z} + \begin{bmatrix} 0 \\ \xi(x_2, \dot{x}_2) \end{bmatrix}. \tag{24}$$

We can choose a positive definite matrix $\boldsymbol{P} \in \mathbb{R}^{2\times 2}$ as

$$\boldsymbol{P} = \begin{bmatrix} C_o & 0 \\ 0 & C_o^2 L_o \end{bmatrix} \tag{25}$$

and construct the quadratic Lyapunov function $V = \boldsymbol{z}^T \boldsymbol{P} \boldsymbol{z}/2$. The derivative of this Lyapunov function can be calculated as

$$\dot{V} = \frac{1}{2}\dot{\boldsymbol{z}}^T \boldsymbol{P}\boldsymbol{z} + \frac{1}{2}\boldsymbol{z}^T \boldsymbol{P}\dot{\boldsymbol{z}}. \tag{26}$$

Substituting (24) into (26) gives

$$\dot{V} = \frac{1}{2}\dot{\boldsymbol{z}}^T \left(\boldsymbol{A}_c^T \boldsymbol{P} + \boldsymbol{P}\boldsymbol{A}_c\right)\boldsymbol{z} + \boldsymbol{z}^T \boldsymbol{P} \begin{bmatrix} 0 \\ \xi(x_2, \dot{x}_2) \end{bmatrix}. \tag{27}$$

For the matrix $\boldsymbol{A_c}$ satisfying the restriction (20), it can be easily proved that

$$\boldsymbol{A}_c^T \boldsymbol{P} + \boldsymbol{P}\boldsymbol{A}_c \leq -\mu \boldsymbol{P}. \tag{28}$$

Substituting (28) into (27) yields

$$\dot{V} \leq -\mu V + \psi(x_2, \dot{x}_2) \tag{29}$$

where

$$\psi(x_2, \dot{x}_2) = -\frac{\rho^2(x_2, \dot{x}_2)}{4\varepsilon}\left(C_o^2 L_o \dot{x}_2\right)^2 + C_o^2 L_o \dot{x}_2 \Delta f(x_2, \dot{x}_2). \tag{30}$$

Since the uncertainty term $\Delta f(x_2, \dot{x}_2)$ satisfies the boundary condition (16), it follows that:

$$\psi(x_2, \dot{x}_2) \leq -\frac{\rho^2(x_2, \dot{x}_2)}{4\varepsilon}\left(C_o^2 L_o \dot{x}_2\right)^2 + \rho(x_2, \dot{x}_2)\left|C_o^2 L_o \dot{x}_2\right|. \tag{31}$$

Let $\sigma = \rho(x_2, \dot{x}_2)|C_o^2 L_o \dot{x}_2|$. From the inequality $(\sigma + 2\varepsilon)^2 \geq 0$, it can be easily obtained that

$$\sigma - \frac{\sigma^2}{4\varepsilon} \leq \varepsilon. \tag{32}$$

Applying the inequality (32) to (31) yields $\psi(x_2, \dot{x}_2) \leq \varepsilon$. Combined with (29), it can be proved that

$$\dot{V} \leq -\mu V + \varepsilon. \tag{33}$$

By multiplying both sides of (33) by $e^{\mu\tau}$, and solving the definite integral over the interval $[0, t]$, we obtain

$$V(t)e^{\mu t} - V(0) \leq \frac{\varepsilon}{\mu} e^{\mu t} - \frac{\varepsilon}{\mu} \tag{34}$$

which can be rewritten as

$$V(t) \leq V(0)e^{-\mu t} + \frac{\varepsilon}{\mu}(1 - e^{-\mu t}). \tag{35}$$

As $t \to \infty$, the Lyapunov function satisfies

$$\lim_{t\to\infty} V(t) \leq \frac{\varepsilon}{\mu}. \tag{36}$$

This indicates that by applying the robust control law (21), the system states are asymptotically driven into the convergence

region

$$\Omega = \left\{ (x_2, \dot{x}_2) \left| \frac{1}{2} C_o (x_2 - x_2^*)^2 + \frac{1}{2} C_o^2 L_o (\dot{x}_2)^2 \le \frac{\varepsilon}{\mu} \right. \right\}. \tag{37}$$

According to the converter model in (1), when the output voltage v_c is stabilized, it has $\mathrm{d}v_c / \mathrm{d}t = 0$, and the inductor current i_L reaches its steady-state value i_L^*, which is determined by the load current i_o and can be calculated as

$$i_L^* = i_o = \frac{v_c}{R} + \frac{P}{v_c}. \tag{38}$$

It is important to note that the steady-state current i_L^* is not a constant but a variable that depends on the output voltage and load conditions at steady state. When the output voltage or load conditions change, i_L^* also varies.

Introducing (38) into the second equation of (1) yields

$$\dot{x}_2 = \dot{v}_c = \frac{1}{C}(i_L - i_L^*). \tag{39}$$

This equation gives the relationship between the tracking error of the inductor current and the rate of change $\dot{v}_c$ of the output voltage.

According to (24), the proposed converter derives the state $z = [\dot{e}\ e]^T = [\dot{v}_c\ \ v_c - v_c^*]^T$ asymptotically and exponentially converge to a sufficiently small neighborhood around the zero point. This ensures that the output voltage v_c tracks its reference value v_c^* and that the inductor current i_L tracks its steady-state value i_L^*, without requiring the detailed load information which determines i_L^*. This feature eliminates the need for additional current sensors to detect the load current under varying load conditions.

By substituting (39) into (37), which describes the convergence domain in terms of the output voltage v_c and its derivative $\dot{v}_c$, the convergence domain can be rewritten as

$$\Omega^* = \left\{ (v_c, i_L) \left| \frac{1}{2} C_o (v_c - v_c^*)^2 + \frac{C_o^2}{2C^2} L_o (i_L - i_L^*)^2 \le \frac{\varepsilon}{\mu} \right. \right\}. \tag{40}$$

This representation describes convergence domain in relation to the output voltage v_c and the inductor current i_L. This transformation facilitates the representation of the convergence domain within phase portraits and the design of convergence domain parameters.

As shown in the phase trajectory of the converter under the proposed robust controller in Fig. 4, the system states are globally stable and asymptotically converge to an elliptical region near the desired operating point.

IV. Parameter Design of the Proposed Controller

In this section, an uncertainty boundary estimator is proposed to estimate the absolute boundary $\rho(x_2, \dot{x}_2)$ of the nonlinear uncertainty term $\Delta f(x_2, \dot{x}_2)$. Based on the physical characteristics of the converter and practical design constraints, the procedure for designing the closed-loop parameters A_1, A_0, and convergence domain parameters μ and ε is then presented to ensure sufficient tracking accuracy and dynamic response.

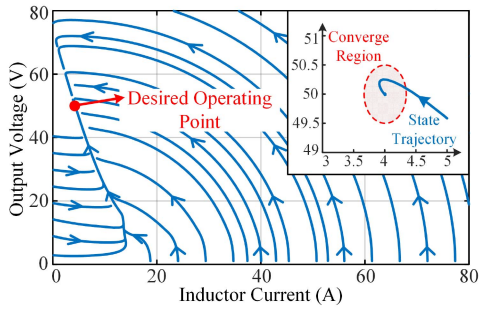

Fig. 4. Phase trajectory of buck converter under the proposed robust controller.

Subsequently, a feasible implementation of the control system using a simple differential state observer is provided.

A. Estimation of Absolute Boundary $\rho(x_2, \dot{x}_2)$

In practice, the converter operates over a given range of input voltage, resistive load, and constant power load. Due to the basic principle of PWM modulation, the duty cycle as a control input satisfies $0 \le u \le 1$. In addition, the parametric tolerances of the passive components L and C are within a fixed range. Consequently, the nonlinear uncertainty term $\Delta f(x_2, \dot{x}_2)$ is bounded, and there exists a positive definite scalar function $\rho(x_2, \dot{x}_2)$ to describe its absolute boundary.

The equation of the nonlinear uncertainty term $\Delta f(x_2, \dot{x}_2)$ has been derived as (10) in Section II. Substituting (4) and the differential of (4) in to (10) gives

$$\begin{aligned} \Delta f(x_2, \dot{x}_2) = &\left(\frac{E}{CL} - \frac{E_o}{C_o L_o} \right) u - \left(\frac{1}{CL} - \frac{1}{C_o L_o} \right) x_2 \\ &- \left(\frac{1}{CR} - \frac{1}{C_o R_o} \right) \dot{x}_2 + \left(\frac{P}{C} - \frac{P_o}{C_o} \right) \frac{\dot{x}_2}{x_2^2}. \end{aligned} \tag{41}$$

According to the basic operating principle of the buck converter, the output voltage always satisfies $0 \le x_2 \le E$. Applying the absolute value inequality $|a \pm b| \le |a| + |b|$ to (41), it can be obtained that

$$\begin{aligned} \|\Delta f(x_2, \dot{x}_2)\| \le &\left| \frac{E}{CL} - \frac{E_o}{C_o L_o} \right| + \left| \frac{1}{CL} - \frac{1}{C_o L_o} \right| x_2 \\ &+ \left| \frac{1}{CR} - \frac{1}{C_o R_o} \right| |\dot{x}_2| + \left| \frac{P}{C} - \frac{P_o}{C_o} \right| \frac{|\dot{x}_2|}{x_2^2}. \end{aligned} \tag{42}$$

For a given range $[E_{\min}, E_{\max}]$ of input voltage E, the nominal value is selected as $E_o = (E_{\min} + E_{\max})/2$. Considering the $\pm 20\%$ parameter tolerance of L and C, the first term of (42) can be estimated as

$$\left| \frac{E}{CL} - \frac{E_o}{C_o L_o} \right| \le \frac{E_{\max}}{C_{\min} L_{\min}} - \frac{E_o}{C_o L_o} = \frac{17 E_{\max} - 8 E_{\min}}{16 C_o L_o}. \tag{43}$$

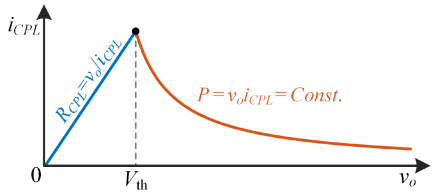

Fig. 5. $I-U$ characteristic of a practical constant power load.

Similarly, the second term of (42) can be estimated as

$$\left|\frac{1}{CL}-\frac{1}{C_oL_o}\right|x_2\le\left(\frac{1}{C_{\min}L_{min}}-\frac{1}{C_oL_o}\right)x_2=\frac{9}{16C_oL_o}x_2. \tag{44}$$

For a given range $[R_{\min},R_{\max}]$ of the resistive load R, the nominal value can be selected as $R_o=2(R_{\max}//R_{\min})=2R_{\max}R_{\min}/(R_{\max}+R_{\min})$. Therefore, the third term of (42) is estimated as

$$\begin{aligned}\left|\frac{1}{CR}-\frac{1}{C_oR_o}\right||\dot{x}_2|&\le\left(\frac{1}{C_{\min}R_{\min}}-\frac{1}{C_oR_o}\right)|\dot{x}_2|\\&=\frac{3R_{\max}-2R_{\min}}{4C_oR_{\min}R_{\max}}|\dot{x}_2|.\end{aligned} \tag{45}$$

Similarly, for a given range $[P_{\min},P_{\max}]$ of constant power load P, the nominal value is selected as $P_o=(P_{\min}+P_{\max})/2$. The last term of (42) can be estimated as

$$\left|\frac{P}{C}-\frac{P_o}{C_o}\right|\frac{|\dot{x}_2|}{x_2^2}\le\left(\frac{P_{\max}}{C_{\min}}-\frac{P_o}{C_o}\right)\frac{|\dot{x}_2|}{x_2^2}\le\frac{3P_{\max}-2P_{\min}}{4C_oV_{\text{th}}^2}|\dot{x}_2| \tag{46}$$

where V_{th} represents the startup threshold voltage of the CPL.

It should be noted that most practical CPLs exhibit positive incremental impedance characteristics during the startup phase, where the load current increases linearly to avoid excessive surge current, as shown in Fig. 5. Once the load voltage reaches the startup threshold voltage V_{th}, the load switches to the constant power phase [30]. The last term of (42) represents the absolute error between the slope of the constant power load current and its nominal value, reaching its maximum at $v_o=V_{\text{th}}$.

By introducing (43), (44), (45), and (46) into (42), the uncertainty boundary estimator can be formulated as a positive continuous scalar function $\rho(x_2,\dot{x}_2)$, which describes the absolute boundary of the uncertain term $\Delta f(x_2,\dot{x}_2)$ and can be calculated as

$$\begin{aligned}\rho(x_2,\dot{x}_2)=&\frac{17E_{\max}-8E_{\min}}{16C_oL_o}+\frac{9}{16C_oL_o}x_2\\&+\left(\frac{3R_{\max}-2R_{\min}}{4C_oR_{\min}R_{\max}}+\frac{3P_{\max}-2P_{\min}}{4C_oV_{\text{th}}^2}\right)|\dot{x}_2|.\end{aligned} \tag{47}$$

It should be noted that the boundary estimation function (47) is a function of the system states x_2 and $\dot{x}_2$ themselves, rather than their maximum or minimum values. Since the nonlinear uncertain term $\Delta f(x_2,\dot{x}_2)$ is a dynamic term dependent on the system states, selecting the boundary estimation function in this form allows for an accurate capture of the upper bound of this dynamic component caused by uncertainty. Moreover, fully utilizing the known state information not only results in less conservative boundary estimates, but also expands the range over which the boundary constraint (16) holds, thus ensuring the global asymptotic stability of the proposed robust controller.

B. Closed-Loop Parameters A_1 and A_0

By applying the proposed robust controller, the closed-loop dynamics approximately follow the desired linear system (13). The parameters A_1 and A_0 not only affect the stability, but also the dynamic response of the closed-loop system.

First, according to *Routh–Hurwitz criterion*, to ensure the stability of the closed-loop system, the parameters A_1 and A_0 must satisfy

$$A_1>0,\ A_0>0. \tag{48}$$

This condition ensures that there are no closed-loop poles located in the positive part of the complex plane, thereby guaranteeing the existence of a positive number μ that satisfies (20). Consequently, the system is stable and the states converges globally asymptotically to the region (40).

In practice, the input dynamics of tightly regulated load converters, which function as CPLs, are typically slower than those of ideal CPLs. As a result, stability boundary analyses based on the simplified ideal CPL model tend to be more conservative [36]. To address this limitation, Appendix A provides a conservatism-free parameter stability region analysis for the proposed controller, accounting for the actual dynamics of the load converter. This refined analysis further relaxes the parameter constraints in (48), offering an extended and more accurate stability boundary for controller design.

Second, the design of the parameters A_1 and A_0 can be achieved using the pole configuration method of linear systems. According to the classical control theory [31], the eigenvalues $\lambda_{1,2}$ of a second-order system are determined as

$$\lambda_{1,2}=\omega_n\left(-\zeta\pm\sqrt{\zeta^2-1}\right) \tag{49}$$

where ζ is the damping ratio and ω_n is the natural resonance frequency of the second-order system.

The damping ratio ζ determines the type of system dynamic response, including overdamped ($\zeta>1$), critically-damped ($\zeta=1$) and underdamped ($0<\zeta<1$). To ensure an output with no overshoot and a faster response, critical damping ($\zeta=1$) is often chosen.

The natural resonance frequency ω_n determines the speed of system's dynamic response. The settling time t_s (with a 2% criterion) of a second-order system can be calculated as

$$t_s=\frac{4.4}{\zeta\omega_n} \tag{50}$$

which means under the same condition of damping ratio ζ, a larger resonance frequency ω_n leads to a faster dynamic response of the system. The trajectories of eigenvalues with the increasing of ζ and ω_n is shown in Fig. 6, and the desired eigenvalues can be determined based on (49) and (50).

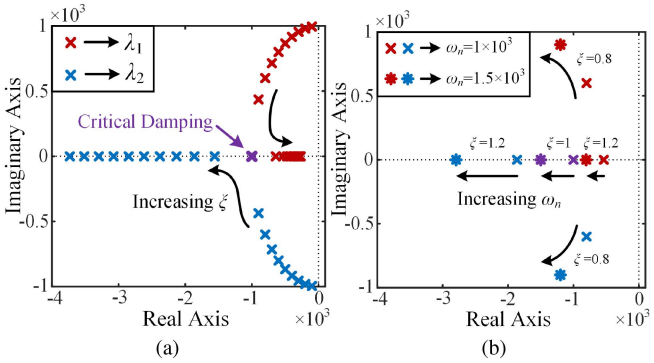

Fig. 6. Trajectories of Eigenvalues: (a) With the increasing of ζ, (b) With the increasing of ω_n.

It is important to note that while a larger natural resonant frequency ω_n implies a faster closed-loop dynamic response, there are limits to its selection. To ensure effective control in power electronic converters, the voltage loop bandwidth (i.e., closed-loop cutoff frequency f_v) is typically designed to be less than 1/50 of the switching frequency f_s, leading to the constraint $f_v \le f_s/50$. This can be expressed in terms of angular frequency as $\omega_v \le \pi f_s/25$. For a second-order system, the relationship between the closed-loop cutoff frequency ω_v and the natural resonance frequency ω_n is given by

$$\omega_v = \omega_n \left(1 - 2\zeta^2 + \sqrt{2 - 4\zeta^2 + 4\zeta^4}\right)^{1/2}. \tag{51}$$

Therefore, the design constraint for ω_n can be expressed as

$$\omega_n \le 0.04\pi f_s / \left(1 - 2\zeta^2 + \sqrt{2 - 4\zeta^2 + 4\zeta^4}\right)^{1/2}. \tag{52}$$

Finally, given the desired eigenvalues $\lambda_{1,2}$, the parameters A_1 and A_0 can be calculated as

$$A_1 = -(\lambda_1 + \lambda_2),\ A_0 = \lambda_1\lambda_2. \tag{53}$$

It should be noted that although the proposed controller does not directly utilize the inductor current signal to form an explicit inner current loop, it cannot be regarded as a conventional single voltage loop control. In conventional single voltage loop control, the voltage loop bandwidth is typically set lower to ensure effective current tracking. This is because the absence of an inner-loop current regulator limits the bandwidth of inductor current response, which is completely determined by the power stage dynamics. In contrast, the proposed controller leverages the system's differential dynamics, as described in (39), which indicate that the differential of the output voltage is proportional to the tracking error of the inductor current. Consequently, the feedback related to $\dot{v}_c$ in the controller can be regarded as implicitly introducing an "equivalent inner current loop", which enables the inductor current to exhibit a fast dynamic response similar to that under dual-loop control. This permits a higher voltage loop bandwidth to obtain a faster system dynamic response. Nonetheless, to suppress high-frequency switching noise and maintain the accuracy of the PWM modulator, adherence to the design constraint specified in (52) remains essential.

C. Convergence Domain Parameters μ and ε

The stability analysis in Section III has proved that the system states will asymptotically converge to the elliptical region Ω^* under the proposed controller. Since the size of convergence region is determined by the parameters μ and ε, it is necessary to appropriately design these parameters to achieve accurate voltage tracking and desired static performance of closed-loop systems.

Once the parameters A_1 and A_0 are determined, according to the constraint (20), the convergence domain parameter μ can be selected as

$$\begin{cases} 0 < \mu < A_1 - \sqrt{A_1^2 - 4A_0}, & A_1 > 2\sqrt{A_0} \\ 0 < \mu < A_1, & A_1 \le 2\sqrt{A_0}. \end{cases} \tag{54}$$

According to the design requirements of the buck converter, the tracking error between the output voltage and its rated value is generally limited to 5%. This condition can be expressed as

$$|v_c - v_c^*| \le 0.05 v_c^*. \tag{55}$$

When the buck converter operates in CCM, the absolute error between the inductor i_L and its steady-state dc component i_L^* is less than half of the peak-to-peak ripple current ΔI_{Lp-p}. This gives the restrictive condition

$$|i_L - i_L^*| \le \frac{1}{2}\Delta I_{Lp-p} = \frac{(E - v_c^*)v_c^*}{2Ef_sL} \le \frac{(E_{\max} - v_c^*)v_c^*}{1.6E_{\max}f_sL_o}. \tag{56}$$

By introducing (55) and (56) into (40), the design rule for the ratio between ε and μ should satisfy

$$0 < \frac{\varepsilon}{\mu} \le \frac{C_o(0.05v_c^*)^2}{2} + \frac{[(E_{\max} - v_c^*)v_c^*]^2}{2 \times 0.8^2 \times (1.6E_{\max}f_s)^2 L_o}. \tag{57}$$

The convergence region parameter ε can be determined by combining (54) and (57).

D. Implementation of the Control System

According to the proposed control law (21), obtaining the differential of the output capacitor voltage is essential for state feedback control. When employing the direct sensing method, the use of a noise-sensitive differentiator becomes inevitable, thereby diminishing the antiinterference and reliability of the entire control system. To address this issue, the indirect method is adopted, wherein the differential of the output capacitor voltage is obtained by sensing the capacitor current i_c and applying the following differential state observer:

$$\hat{\dot{x}}_2 = \frac{1}{C_o} i_c \tag{58}$$

where $\hat{\dot{x}}_2$ represents the observed value of $\dot{x}_2$ under the proposed method.

The actual value can be deduced as $\dot{x}_2 = i_c/C$. Combining this with (58) gives the relationship between the observed value and actual value as $\hat{\dot{x}}_2 = (C/C_o)\dot{x}_2$. Therefore, the presence of parameter tolerance of C may result in a certain amount of detection error, which has four impacts on the closed-loop control system.

First, the controller cannot completely compensate for the known open-loop nonlinear term $f(x_2, \dot{x}_2)$, wherein the difference can be processed as a new uncertain term in $\Delta f(x_2, \dot{x}_2)$. Therefore, the absolute boundary function $\rho(x_2, \dot{x}_2)$ should include an additional term

$$\left|\frac{C_o - C}{C_o}\left(\frac{1}{R_o C_o} - \frac{P_o}{C_o x_2^2}\right)\right| \times |\dot{x}_2| \le \left(\frac{0.25}{R_{\min} C_o} + \frac{0.25 P_{\max}}{C_o V_{\text{th}}^2}\right)|\dot{x}_2| \tag{59}$$

and $\rho(x_2, \dot{x}_2)$ can be revised as

$$\rho(x_2, \hat{\dot{x}}_2) = \frac{17E_{\max} - 8E_{\min}}{16 C_o L_o} + \frac{9}{16 C_o L_o} x_2 + \left(\frac{2R_{\max} - R_{\min}}{2C_o R_{\min} R_{\max}} + \frac{2P_{\max} - P_{\min}}{2C_o V_{\text{th}}^2}\right)\frac{|\hat{\dot{x}}_2|}{0.8}. \tag{60}$$

Second, the eigenstructure of the closed-loop system may deviate from the desired value. The actual closed-loop system dynamics are approximated by the following linear system:

$$\ddot{e} + \frac{C}{C_o} A_1 \dot{e} + A_0 e = 0. \tag{61}$$

When A_1 and A_0 are designed to operate at critical damping, if $C < C_o$, the actual closed-loop system operates at under damping, resulting in an overshoot in the output dynamic response. To ensure the overshoot-free regulation, margins should be considered in the design of the parameter A_1. Therefore, a damping ratio of $\zeta \ge 1/0.8 = 1.25$ is selected in the process of designing closed-loop parameters A_1 and A_0.

Third, due to the parameter tolerance of C, applying the state observer (58) may lead to a rightward shift of the pole near the imaginary axis. When the design constraint $\zeta \ge = 1.25$ is satisfied, it follows that $1.2A_1 > 2\sqrt{A_0}$. To ensure the global asymptotic stability of the closed-loop system, the parameter design range for μ should be tightened to

$$0 < \mu < 1.2A_1 - \sqrt{(1.2A_1)^2 - 4A_0}. \tag{62}$$

Fourth, affected by the observer error, the actual convergence domain becomes

$$\Omega^* = \left\{(v_c, i_L)\,\middle|\, \frac{C_o}{2}(v_c - v_c^*)^2 + \frac{C_o^2}{2C^2} L_o (i_L - i_L^*)^2 \le \frac{C_o \varepsilon}{C\mu}\right\}. \tag{63}$$

To ensure that the convergence domain satisfies the design requirements (55) and (56), the design interval (57) for ε/μ should be multiplied by a correction factor of 0.8, and becomes

$$0 < \frac{\varepsilon}{\mu} \le \frac{C_o (0.05 v_c^*)^2}{2.5} + \frac{[(E_{\max} - v_c^*) v_c^*]^2}{2 \times 0.8 \times (1.6 E_{\max} f_s)^2}. \tag{64}$$

It is worthy noting that if the differentiator direct sensing method is used, the abovementioned parameter corrections do not need to be taken into account. In addition to this, the state observer can also be chosen as

$$\hat{\dot{x}}_2 = \frac{x_1}{C_o} - \frac{x_2}{C_o R_o} - \frac{P_o}{C_o x_2} \tag{65}$$

and parameters corrections should also be considered according to the observer error. This option is not discussed further in this article. The block diagram of the proposed HOFA-based robust controller is depicted in Fig. 7.

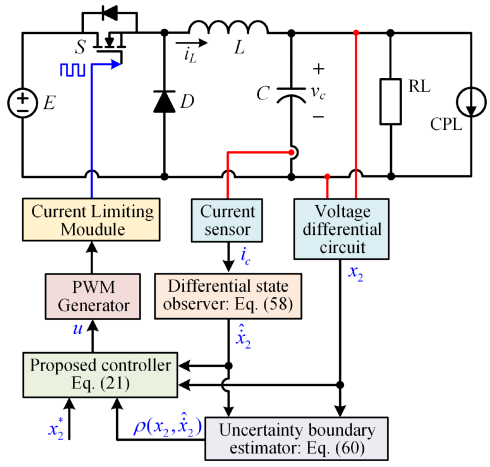

Fig. 7. Block diagram of the proposed HOFA-based robust controller.

E. Design of the Current Limiting Module

Overcurrent protection is crucial in converters to prevent component damage during transients, where current surges may occur. Proper current limitation not only safeguards the converter switches from catastrophic failures, but also ensures the overall reliability and longevity of the system.

Unlike the approach in [19], which implements current limiting through a complex inequality constraint on the duty cycle in model predictive control, and the solutions in [14] and [32], which introduce a current saturation limit before the inner-loop current reference, this paper proposes a novel current limiting method. In this method, the inductor current i_L is indirectly limited by constraining the capacitor current i_c, eliminating the need for additional current sensors.

According to the converter model (1), the relationship between the inductor and capacitor currents is given by

$$i_L = i_c + i_o \tag{66}$$

where $i_o = v_c/R + P/v_c$ represents the load current. Since the load current is bounded ($0 \le i_o \le i_{o,\max}$), the inductor current can be indirectly limited by constraining the capacitor current.

Assuming the capacitor current is limited to $i_{c,\lim}$, the inductor current is then constrained by $i_{L,\lim} = i_{c,\lim} + i_o$. If the desired overcurrent protection limit for the inductor current is a constant I_{ocp}, then the capacitor current limit $i_{c,\lim}$ should be designed as $i_{c,\lim} = I_{\text{ocp}} - i_o$. However, without an additional current sensor, the load current i_o cannot be accurately measured. To address this, the proposed method roughly estimates the load current using the nominal values of the load parameters R_o, P_o and the detected output voltage v_c, which can be calculated as

$$i_o^* = \begin{cases} \frac{v_c}{R_o} + \frac{P_o}{v_c}, & \text{if } v_c > V_{\text{th}} \\ \frac{v_c}{R_o} + \frac{P_o}{V_{\text{th}}^2} v_c, & \text{if } v_c \le V_{\text{th}}. \end{cases} \tag{67}$$

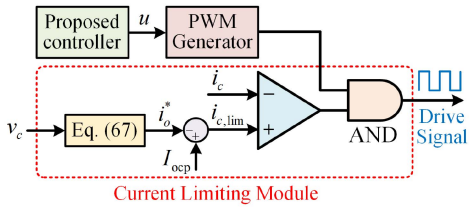

Fig. 8. Schematic diagram of the current limiting module for the proposed controller.

The limiting value of i_c is then designed as

$$i_{c,\lim} = I_{\text{ocp}} - i_o^*. \tag{68}$$

Substituting (68) into (66), the inductor current limit becomes

$$i_{L,\lim} = I_{\text{ocp}} - i_o^* + i_o. \tag{69}$$

It is evident from (69) that the proposed method allows the inductor current limit $i_{L,\lim}$ to fluctuate around I_{ocp}, depending on the actual load conditions. As the load increases, the current limit correspondingly increases; conversely, as the load decreases, the current limit decreases accordingly. This adaptive behavior is acceptable in practice, provided that the maximum limiting value does not exceed the maximum current rating of the components, and the minimum limiting value is sufficient for normal operation.

The implementation of the proposed overcurrent protection method is illustrated in Fig. 8. The detected capacitor current i_c is compared with the capacitor current limit $i_{c,\lim}$ using a comparator. The pulse-width modulated control signal u and the output of the comparator are then fed into an AND gate to generate the drive signal for the switch S. When the capacitor current i_c exceeds its limit $i_{c,\lim}$, the drive signal is forced to a low level, causing the inductor current i_L decrease ($\mathrm{d}i_L/\mathrm{d}t < 0$) until it falls below the limit, thereby achieving effective overcurrent protection.

Based on the given nominal load parameters R_o and P_o in Subsection A of this section, the nominal value of the load current can be calculated as

$$i_o^* = (i_{o,\min} + i_{o,\max})/2. \tag{70}$$

Substituting (70) into (69), the range of the inductor current limit $i_{L,\lim}$ can be determined as

$$I_{\text{ocp}} + (i_{o,\min} - i_{o,\max})/2 \le i_{L,\lim} \le I_{\text{ocp}} + (i_{o,\max} - i_{o,\min})/2. \tag{71}$$

To prevent overcurrent damage to the components, the maximum inductor current limit should be designed to be less than the maximum current withstand $I_{\max}$ of the components. This gives the design constraint

$$I_{\text{ocp}} + (i_{o,\max} - i_{o,\min})/2 < I_{\max}. \tag{72}$$

In addition, the inductor current limit $i_{L,\lim}$ should always be greater than the load current i_o to ensure that the constant power load can startup properly. If this condition is not met, the converter will operate at the current-limiting point, which

TABLE I
SIMULATION AND EXPERIMENTAL PARAMETERS OF THE BUCK CONVERTER

Descriptions	Symbols	Parameter values
Input voltage	E	60~80 V
Desired output voltage	v_c^*	50 V
Inductance	L	2 mH ± 20%
Capacitance	C	470 μF ± 20%
Resistive load	R	50~∞ Ω
Constant power load	P	0~150 W
Switching frequency	f_s	20 kHz

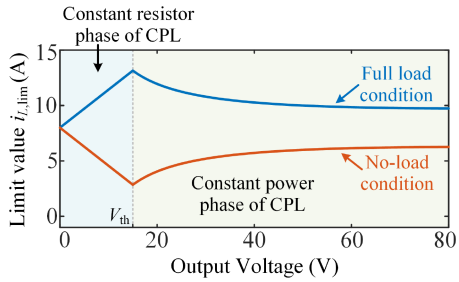

Fig. 9. Curves of inductor current limit $i_{L,\lim}$ with the variety of output voltage v_c under different load conditions.

gives another design constraint

$$I_{\text{ocp}} - i_o^* + i_o > i_o. \tag{73}$$

In dc microgrids where CPLs dominate the load system, the peak values of i_o^* and $i_{o,\max} - i_{o,\min}$ occur at the startup threshold voltage V_{th}. By combining (72) and (73), and substituting $v_c = V_{\text{th}}$, the design rule for I_{ocp} can be derived as

$$\frac{V_{\text{th}}}{R_o} + \frac{P_o}{V_{\text{th}}} < I_{\text{ocp}} < I_{\max} + \frac{V_{\text{th}}(R_{\min} - R_{\max})}{2R_{\min}R_{\max}} + \frac{P_{\min} - P_{\max}}{2V_{\text{th}}}. \tag{74}$$

Using the system parameters outlined in Table I, and assuming a maximum current rating of $I_{\max} = 20$ A and the startup threshold voltage of the CPL at $V_{\text{th}} = 15$ V, substituting these values into (74) yields the design constraint $5.15\ \text{A} < I_{\text{ocp}} < 14.85\ \text{A}$. By selecting $I_{\text{ocp}} = 8$ A for the proposed current limiting circuit, the curves depicting the inductor current limit $i_{L,\lim}$ with the variety of output voltage v_c under different load conditions are presented in Fig. 9.

V. SIMULATION RESULTS

In this section, a simulation model of a buck converter feeding hybrid loads (RL+CPL), which implements the proposed control algorithm, is developed using MATLAB/Simulink to demonstrate the effectiveness of the proposed HOFA-based robust controller. The parameters of the buck converter used for both simulation and experimental validation are listed in Table I.

To verify the dynamic performance and robustness during load, input or output reference sudden changing of the proposed method, the comparison has been made between the cascaded PI controller, the passivity-based controller with nonlinear disturbance observer (PBC+NDO) [10] and this proposed HOFA-based robust controller.

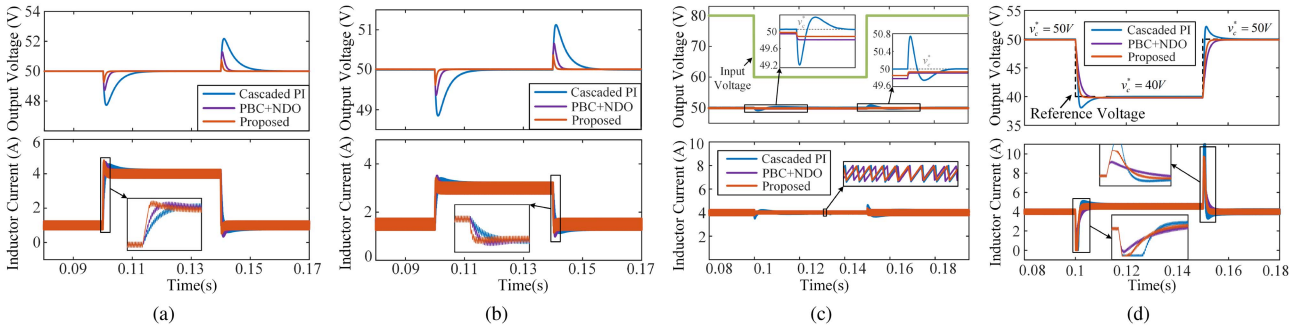

Fig. 10. Simulated dynamic response of output voltages and inductor currents when: (a) Output power step change in CPL from 0 to 150 W at $t = 0.1$ s, and from 150 to 0 W at $t = 0.14$ s, with a 50 Ω constant resistive load, (b) Output power step change in CPL from 75 to 150 W at $t = 0.1$ s, and from 150 to 75 W at $t = 0.14$ s, without resistive load, (c) Input voltage step change from 80 to 60 V at $t = 0.1$ s, and from 60 to 80 V at $t = 0.15$ s, (d) Output voltage reference step change from 50 to 40 V at $t = 0.1$ s, and from 40 to 50 V at $t = 0.15$ s.

The parameters of the proposed controller can be calculated according to the design procedures proposed in Section IV. The nominal values of the system parameters are $E_o = 70$ V, $R_o = 100\,\Omega$ and $P_o = 75$ W. Setting $V_{\text{th}} = 15$ V, the absolute boundary function can be determined as

$$\rho(x_2, \dot{x}_2) = 3.02 \times 10^7 + 3.09 \times 10^5 x_2 + 9.43 \times 10^2 |\dot{x}_2|. \tag{75}$$

Choosing the natural resonance frequency $\omega_n = 5 \times 10^3$ and critical damping ratio $\zeta = 1.25$, the closed-loop parameters A_1 and A_0 can be calculated by

$$A_1 = 1.25 \times 10^4,\ A_0 = 2.5 \times 10^7. \tag{76}$$

According to (62), the parameter μ can be determined as $\mu = 3.82 \times 10^3$. Combining with (64) and the selected μ, the parameter ε can be calculated as $\varepsilon = 49$. Then, the control law can be obtained by taking the above parameters into (21).

Under the same main circuit parameters listed in Table I, the cascaded PI controller used for comparison is designed according to the standard design guidelines outlined in [20]. This approach is based on the linearized model in the frequency domain, aiming to achieve the desired dynamic performance while ensuring sufficient stability margins. For a fair comparison, the bandwidth ω_v of the outer voltage loop is selected to match the control bandwidth of the proposed controller, calculated as $\omega_v = \omega_n(1 - 2\zeta^2 + \sqrt{2 - 4\zeta^2 + 4\zeta^4})^{1/2} = 2364$ rad/s. Consequently, the control parameters for the outer voltage loop can be determined as $K_{pv} = 1.11$ and $K_{iv} = 263$. To ensure effective cascaded-loop control, the bandwidth of the inner current loop is set to ten times that of the outer voltage loop, resulting in $\omega_i = 2.364 \times 10^4$ rad/s, with control parameters $K_{pi} = 0.68$ and $K_{ii} = 1600$.

For the comparison with the PBC+NDO, we adopt the gain selection technique proposed in [33] to design the virtual resistances R_{1d} and R_{2d} of the PBC, ensuring a fair comparison and the best performance. The natural resonance frequency ω_n and damping ratio ξ of the desired closed-loop system are aligned with those of the proposed controller. The control parameters for the PBC are set as $R_{1d} = 26.33$ and $R_{2d} = 1.17$. To optimize the observer's performance, we apply the standard design procedure from [34] to determine the gain parameters λ_1 and λ_2 of the NDO, which are established as $\lambda_1 = 8128$ and $\lambda_2 = 1700$.

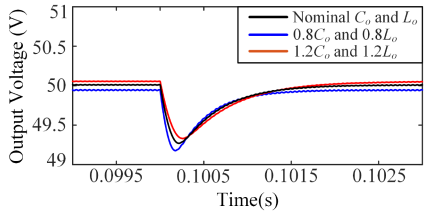

Fig. 11. Simulated dynamic response of output voltages when CPL power changes from 0 to 150 W at nominal parameters L_o and C_o, −20% parameter offset and +20% parameters offset.

TABLE II
COMPARISON OF THE SIMULATION RESULTS

Operation conditions		Metrics	Cascaded PI	PBC+NDO	Proposed
CPL power steps	0W→150W	VF	2.27V	1.31V	0.74V
		RT	18.72ms	4.29ms	2.43ms
	150W→0W	VF	2.18V	1.25V	0.69V
		RT	17.64ms	4.17ms	2.42ms
Input voltage steps	80V→60V	O	0.76V	≈0V	≈0V
		SE	≈0V	0.22V	0.15V
	60V→80V	O	0.78V	≈0V	≈0V
		SE	≈0V	94mV	63mV
Reference voltage steps	50V→40V	O	1.94V	≈0V	≈0V
		RT	11.18ms	4.31ms	2.16ms
	40V→50V	O	2.08V	≈0V	≈0V
		RT	12.20ms	4.57ms	2.46ms

Notes: VF: Voltage fluctuation, RT: Regulation time, O: Overshoot, SE: Static error.

The simulated dynamic responses of output voltages and inductor currents under different controllers in four operation cases are illustrated in Figs. 10 and 11. In addition, the numerical comparison of the simulation results is given in Table II.

A. Case I: CPL Power Changes

In this case, step changes in the CPL power of the buck converter are considered. Fig. 10(a) illustrates the simulation results of the output voltage and the inductor current when a 150 W

CPL is switched ON at $t = 0.1$ s and switched OFF at $t = 0.14$ s, while the converter simultaneously feeds a resistive load of 50 Ω. In addition, Fig. 10(b) presents the simulation results for the output voltage and inductor current under the condition where the CPL power steps from its nominal value of 75 W to its maximum value of 150 W at $t = 0.1$ s and returns to 75 W at $t = 0.14$ s without the resistive load. Comparing the simulation results gives shows that the proposed controller achieves the fastest dynamic recovery performance with the smallest voltage fluctuation under large CPL power changes. The integral term in the cascaded PI controller helps eliminate static errors but worsens the transient performance of the system, leading to larger voltage swings and slower regulation. In addition, the estimated value for the CPL power by the nonlinear disturbance observer applied in PBC+NDO lags behind the actual change values. There is a tradeoff between tracking speed and tracking accuracy in the observer, resulting in a slower dynamic response compared to the proposed controller.

B. Case II: Input Voltage Changes

Fig. 10(c) shows the dynamic response of the converter under input voltage changes. The input voltage steps from 80 to 60 V at $t = 0.1$ s, and returns to 80 V at $t = 0.15$ s. It is observed that, except for the cascaded PI controller, both the proposed controller and PBC+NDO exhibit no significant voltage fluctuation under the 25% input variation. The inclusion of an integral term guarantees the error-free regulation of the cascaded PI controller under different input voltages. Without the integral term, the proposed controller and PBC+NDO exhibit small steady-state errors. However, benefiting from the dynamic compensation on the nonlinear uncertainty terms, the proposed controller can further reduce the static error to achieve better steady-state performance compared with PBC+NDO.

C. Case III: Reference Voltage Changes

Fig. 10(d) shows the simulation results of the output voltage and the inductor current of the buck converter under the step changes of the reference output voltage. The reference voltage steps from 50 to 40 V at $t = 0.1$ s, and from 40 to 50 V at $t = 0.15$ s. Under the 25% reference voltage variation, the proposed controller exhibits less inductor current overshoot while achieving faster dynamic response compared to the cascaded PI controller. This is due to the fact that the integration term in the PI controller adds an extra pole to the system, increasing the system order and introducing additional system dynamics, resulting in larger transient overshoot and slower dynamic response.

D. Case IV: Parameter Mismatch

To validate the robustness of the proposed controller against parameter mismatches in the inductor L and capacitor C from their nominal value L_o and C_o, simulated results of the output voltage v_c during CPL power changes from 0 to 150 W are presented. The simulations were conducted with nominal parameters, as well as with -20% and $+20\%$ offset in the parameters. These results are illustrated in Fig. 11. It can be observed that the dynamic recovery and steady-state performance of the output voltage show minimal differences under $\pm 20\%$ parameter offsets when the proposed controller is applied. This demonstrates the strong robustness of the proposed controller against parameter mismatches.

The above simulated waveforms and comparison results demonstrate that, compared with the cascaded PI controller and PBC+NDO, the proposed control strategy achieves accurate voltage tracking with smaller steady-state error and the superior dynamic performance under the input or load disturbances and reference voltage changes. In addition, the proposed controller shows robust performance against parameter mismatches, further enhancing its reliability in practical applications.

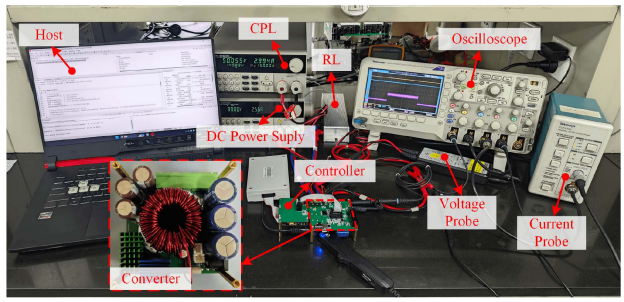

Fig. 12. Experimental platform of buck converter feeding RL and CPL for validating the proposed control method.

VI. Experimental Results

To validate the superiority of the proposed controller, an experimental platform is constructed in the laboratory, as shown in Fig. 12. The proposed control method is implemented on the DSP TMS320F28335 C2000 microcontroller. The programmable power supply IT6722 A is used as the dc input source, and the dc programmable electronic load IT8511A+ operating in the constant power mode is employed to emulate the CPL. The power devices for the main circuit include the MOSFET JCS640RH for active switch S and Schottky diode SRT20L150SCS for diode D. In addition, the current sensor IC ACS733KLATR is used to sense the current of the output filter capacitor C.

The experimental parameters for main circuit are given in Table I, which are the same as the simulation parameters. The control parameters follow the results calculated in Section V. The experimental tests are conducted under the following four conditions:

1) CPL power changes;
2) input voltage changes;
3) reference voltage changes;
4) parameter mismatches.

In each condition, the dynamic response waveforms of the output voltage and inductor current are tested in the experimental platform and captured in an oscilloscope when using the cascaded PI controller and the proposed controller, respectively.

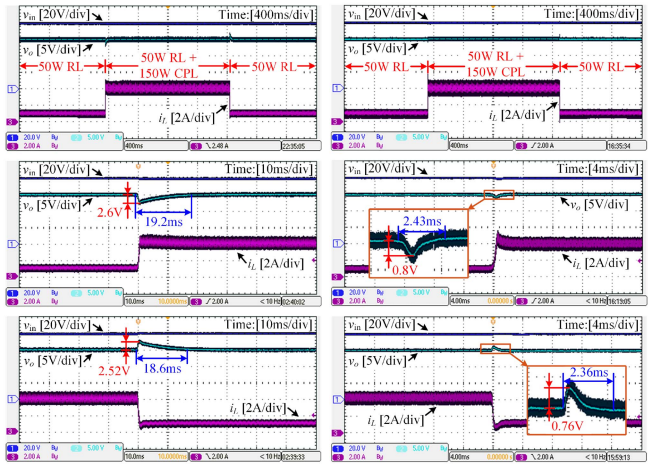

(a) (b)

Fig. 13. Experimental results of system dynamic response under the condition that CPL power changes from 0 to 150 W and back to 0 W with a 50 Ω constant resistive load using: (a) Conventional cascaded PI controller, (b) Proposed HOFA-based robust controller.

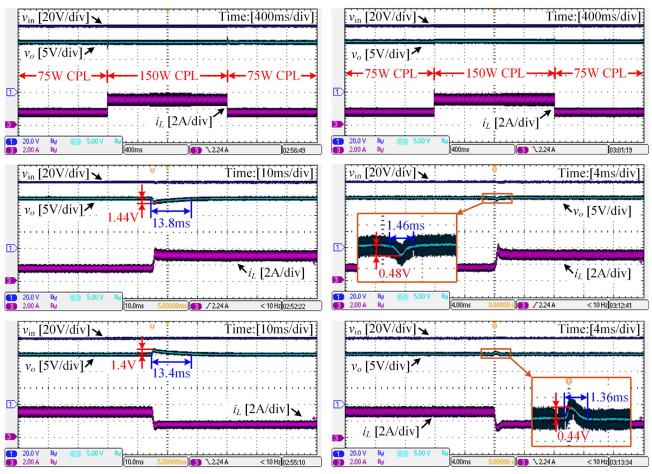

(a) (b)

Fig. 14. Experimental results of system dynamic response under the condition that CPL power changes from 75 to 150 W and back to 75 W without resistive load using: (a) Conventional cascaded PI controller, (b) Proposed HOFA-based robust controller.

A. Experimental Test of CPL Power Changes

Fig. 13(a) and (b) illustrate the system's dynamic response when CPL power transitions from 0 to 150 W and back to 0 W with a 50 Ω constant resistive load, using the conventional cascaded PI controller and the proposed HOFA-based robust controller, respectively. In addition, Fig. 14(a) and (b) show the system's response for CPL power changes from 75 to 150 W and back to 75 W, without the constant resistive load, again comparing the conventional cascaded PI controller with the proposed controller. It can be observed that voltage fluctuation and the regulation time of the output using the proposed HOFA-based robust controller are significantly less than those using the conventional cascaded PI controller. To further validate the superiority of the proposed controller, a numerical comparison of the experimental results under the condition of CPL power variation between the proposed controller and other state-of-the-art control methods is presented in Table III. The comparison results demonstrate the superior dynamic performance of the proposed controller.

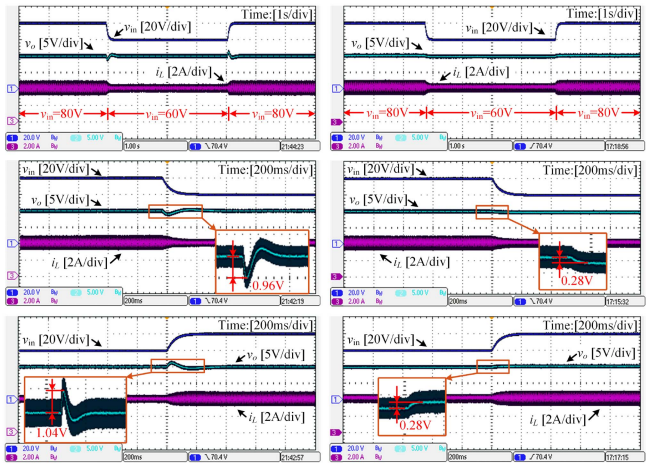

(a) (b)

Fig. 15. Experimental results of system dynamic response under the condition that input voltage changes from 80 to 60 V and back to 80 V using: (a) Conventional cascaded PI controller, (b) Proposed HOFA-based robust controller.

B. Experimental Test of Input Voltage Changes

Fig. 15(a) and (b) depict the system dynamic response under the condition where the input voltage changes from 80 to 60 V and returns to 80 V using conventional cascaded PI controller and the proposed HOFA-based robust controller, respectively. Compared to the cascaded PI controller, the proposed controller achieves a faster and smoother transition of the output voltage without any overshoot, demonstrating the superior robustness against input voltage disturbance. Under the 25% input voltage variation, the output voltage experiences a change of just 0.28 V, which is less than 0.6% of its rated value, illustrating the good steady-state performance of the proposed controller.

C. Experimental Test of Reference Voltage Changes

Fig. 16(a) and (b) show the system dynamic response under the condition where the reference output voltage changes from 50 to 40 V and back to 50 V using the conventional cascaded PI and the proposed HOFA-based robust controller, respectively. It can be observed that with the proposed controller, the output voltage can swiftly, precisely, and steadily track the varied reference output voltage without any overshoot. In contrast, with the cascaded PI controller, the output voltage exhibits significant overshoot, longer settling time and higher current overshoot when tracking the varied reference voltage. This demonstrates the superiority of the proposed method in dynamic response speed and tracking accuracy. In addition, the experimental results demonstrate that the proposed overcurrent limiting module effectively restricts the inductor current to below 10 A during the

TABLE III
COMPARISON OF THE PROPOSED CONTROLLER AND OTHER METHODS

Methods	Number of sensors	Degree of freedom	CPL power variation (W)	Voltage fluctuation (%)	Regulating time (ms)	Overcurrent protection
Backstepping +NDO [17]	2	4	50	8	40	No
Plant-integrating controller [32]	2	2	125	2.9	7	Yes
MPC+NI [19]	3	5	10	8.3	20	Yes
DQSMC [14]	2	4	192	2.5	-	Yes
PBC+NDO [10]	2	4	9.8	2.78	4.5	No
PBC+PO [11]	3	4	60	6.7	7	No
PBC+AEKF [12]	2	3	23.2	4.4	3.6	No
ESC [21]	3	3	20	2.1	200	No
GDPC+NDO [22]	2	6	50	1.3	25	No
Proposed	2	4	150	1.6	2.4	Yes

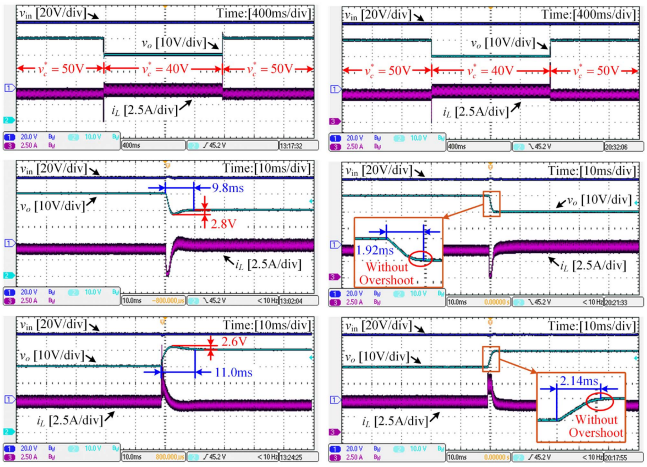

Fig. 16. Experimental results of system dynamic response under the condition that reference voltage changes from 50 to 40 V and back to 50 V using: (a) Conventional cascaded PI controller, (b) Proposed HOFA-based robust controller.

harsh transient condition when a 25% reference voltage variation from 40 to 50 V, which verifies the effectiveness of the proposed current limiting module.

D. Experimental Test of Parameter Mismatch

To evaluate the robustness of the proposed controller against inductance and capacitance parameter mismatches, load step experiments were conducted with CPL power varying from 0 to 150 W under three different circuit parameter conditions: nominal L_o and C_o values, a -20% parameter offset ($0.8L_o$ and $0.8C_o$), and a $+20\%$ parameter offset ($1.2L_o$ and $1.2C_o$). The impact of parameter mismatches on controller performance is demonstrated by comparing the resulting voltage fluctuations and steady-state errors, providing a clear and intuitive assessment. The experimental results in Fig. 17 indicate that the voltage fluctuations across all three parameter conditions remain similar, each below 2% of the rated output. Additionally, the steady-state errors are consistent, remaining within 1% of the rated output.

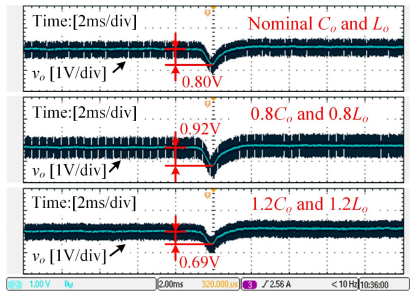

Fig. 17. Experimental results of the proposed controller under the condition that CPL power changes from 0 to 150 W at nominal parameters L_o and C_o, -20% parameter offset and $+20\%$ parameters offset.

This demonstrates that the dynamic recovery and steady-state performance of the proposed controller are maintained despite parameter mismatches, validating its robustness in such scenarios.

In summary, the proposed controller ensures system stability under a wide range of input and load disturbance, achieves accurate voltage tracking, and demonstrates superior dynamic recovery performance and fast response speed. These results are consistent with the theoretical analysis and simulation verification. There is a small difference between the numerical results of the experiment and the simulation. The dynamic response in the experimental case is slightly slower because the voltage of the input power supply and the power of the electronic load cannot be changed instantaneously in the experiment to emulate the desired step change in the simulation. In addition, due to sampling circuit errors and analog-to-digital conversion accuracy, the steady-state error in the experiments is slightly larger than that in the simulation, but this remains within the acceptable range.

VII. CONCLUSION

This article presents a novel robust controller based on HOFA system approach to address the instability problems of buck converters with CPLs in dc microgrid. First, a robust nonlinear control strategy is proposed, derived from the second-order uncertain fully actuated model of the system. An uncertainty

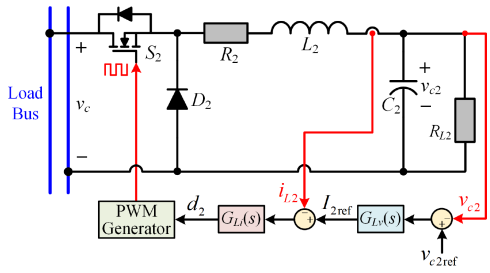

Fig. 18. Control system diagram of the load converter in CPL.

boundary estimator is designed to enhance system robustness against disturbances without precise measurements of power load or input. A simple and easy-to-implement differential state observer is then adopted to avoid the direct use of differentiators. Finally, the effectiveness of the proposed method is validated through simulation and experimental results, demonstrating fast dynamic response, small steady-state error, and strong robustness against the disturbances. The controller achieves accurate output voltage tracking and superior performance compared to existing methods. The HOFA system approach presents a novel and intriguing research direction for the analysis and control of power electronic converters form the perspective of high-order system dynamics, yet many opportunities for further exploration and development remain.

APPENDIX

A. *Conservatism-Free Parameter Stability Region Analysis*

In prior studies, CPLs are often modeled as ideal controlled current sources to simplify controller design. However, this approach neglects the dynamic behavior of actual CPLs, where load converters operate under closed-loop regulation. Due to the slower dynamic response of real CPLs compared to their ideal counterparts, stability conclusions based on simplified models can lead to overly conservative parameter constraints for source converters [36].

To obtain a conservatism-free parameter stability region of the proposed controller while accounting for the actual dynamics of the load converter under tightly regulation, this section studies a buck converter feeding a resistive load as the CPL that connected to the load bus, as shown in Fig. 18. Based on its operational principles, the dynamic model is

$$\begin{cases} L_2 \frac{\mathrm{d}i_{L2}}{\mathrm{d}t} = d_2 v_c - R_2 i_{L2} - v_{C2} \\ C_2 \frac{\mathrm{d}v_{C2}}{\mathrm{d}t} = i_{L2} - \frac{v_{C2}}{R_{L2}}. \end{cases} \tag{77}$$

The closed-loop controller of the load converter consists of an outer voltage loop and an inner current loop, with the transfer functions as $G_{Lv}(s)$ and $G_{Li}(s)$, respectively. The control system can be expressed as

$$\begin{cases} I_{L2\text{ref}} = K_{Lvp}(V_{C2,\text{ref}} - v_{C2}) + K_{Lvi}\int (V_{C2,\text{ref}} - v_{C2})\mathrm{d}t \\ d_2 = K_{Lip}(I_{L2,\text{ref}} - i_{L2}) + K_{Lii}\int (I_{L2,\text{ref}} - i_{L2})\mathrm{d}t \end{cases} \tag{78}$$

where K_{Lvp} and K_{Lvi} are the proportional and integral coefficients of the outer voltage loop, respectively; K_{Lip} and K_{Lii} are the proportional and integral coefficients of the inner current loop, respectively.

The inductor current i_{L2} of the load converter can be derived by solving the differential equation in the first term of (77) as

$$i_{L2} = (d_2 v_c - v_{C2} + k_1 e^{\frac{-R_2}{L_2}t})/R_2 \tag{79}$$

where k_1 is a constant determined by the initial value $i_{L2}(t=0)$ of the inductor current.

Substituting the second equation of (78) into (79), the current i_{L2} under closed-loop regulation can be rewritten as

$$\begin{aligned} i_{L2} = [&K_{Lip} I_{L2,\text{ref}} v_c - v_{C2} + K_{Lii} v_c \int (I_{L2,\text{ref}} - i_{L2})\mathrm{d}t \\ &+ k_1 e^{\frac{-R_2}{L_2}t}]/(R_2 + K_{Lip} v_c). \end{aligned} \tag{80}$$

Assuming negligible energy loss in the load converter, it has $i_{\text{bus}} v_c = i_{L2} v_{C2} = P_{real}$. Therefore, the actual load power of the converter can be calculated as

$$\begin{aligned} P_{\text{real}} = [&K_{Lip} I_{L2,\text{ref}} v_c v_{C2} + K_{Lii} v_c v_{C2} \int (I_{L2,\text{ref}} - i_{L2})\mathrm{d}t \\ &- v_{C2}^2 + k_1 v_{C2} e^{\frac{-R_2}{L_2}t}]/(R_2 + K_{Lip} v_c). \end{aligned} \tag{81}$$

In the proposed controller (21), the term $-B^{-1}P_o \dot{x}_2/(C_o x_2^2)$ compensates for the nonlinear dynamics introduced by CPLs. However, due to the slower dynamic response of the load converter input current ($i_{\text{bus}} \le P_o/v_c$), the actual load power instantaneously processed by the source converter is $P_{\text{real}} \le P_o$. Consequently, the compensatory term overcompensates, leading to the following approximate linear closed-loop system:

$$\ddot{v}_c + A_1 \dot{v}_c + \frac{P_o - P_{\text{real}}}{C_o v_c^2}\dot{v}_c + A_0(v_c - v_c^*) = 0. \tag{82}$$

For this second-order system, stability requires $A_0 > 0$ and

$$A_1 + \frac{P_o - P_{\text{real}}}{C_o v_c^2} > 0. \tag{83}$$

In the load converter's steady state, it has $i_{L2} = I_{L2,\text{ref}}$, $v_{C2} = V_{C2,\text{ref}}$, and $P_o = I_{L2,\text{ref}} V_{C2,\text{ref}}$. In addition, $e^{-R_2 t/L_2} \le 1$ holds for $\forall t \le 0$, and the coefficient k_1 is determined as $k_1 = I_{L2,\text{ref}} R_2$. Substituting these conditions into (81) gives

$$P_{\text{real}} \le P_o - \frac{(V_{C2,\text{ref}} - I_{L2,\text{ref}} R_2) V_{C2,\text{ref}}}{K_{Lip} v_c} \tag{84}$$

where R_2 is the parasitic resistance of the load converter inductor L_2, and it generally satisfies $I_{L2,\text{ref}} R_2 << V_{C2,\text{ref}}$.

Given the permissible fluctuation range of dc bus voltage is $\pm 10\%$ of its rated value ($v_c \le 1.1 \times v_c^*$). The overcompensated part of the proposed controller for the source converter can thus be estimated as

$$\frac{P_o - P_{\text{real}}}{C_o v_c^2} \ge \frac{(V_{C2,\text{ref}} - I_{L2,\text{ref}} R_2) V_{C2,\text{ref}}}{(1.1 \times v_c^*)^3 K_{Lip} C_o}. \tag{85}$$

Substituting (85) into the stability constraint (83), the design constraint of the control parameter A_1 can be relaxed to

$$A_1 > -\frac{(V_{C2,\text{ref}} - I_{L2,\text{ref}} R_2) V_{C2,\text{ref}}}{(1.1 \times v_c^*)^3 K_{Lip} C_o}. \tag{86}$$

For the given parameters: Parasitic resistance $R_2 = 15$ m Ω, rated output voltage $V_{C2,\text{ref}} = 40$ V, rated load power $P_o = 75$

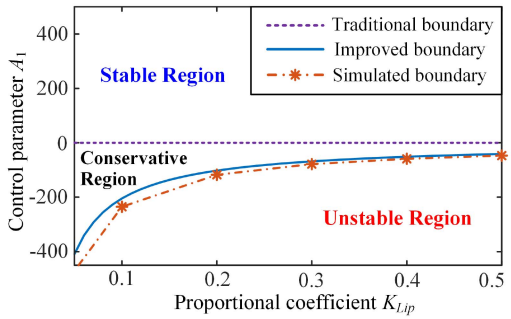

Fig. 19. Stability boundaries for designing the control parameter A_1.

W, rated inductor current $I_{L2,\text{ref}} = P_o/V_{C2,\text{ref}} = 1.875$ A, proportional coefficient $K_{Lip} = 0.1$, output filter capacitor $C_o = 470\ \mu$ F, and the rated dc bus voltage $v_c^* = 50$ V. Substituting these values into the design constraint (86), the parameter stability region of A_1 can be extend to $A_1 > -204.47$. This result considers the actual dynamics of the load converter rather than treating it as an ideal CPL.

It is important to note that the proportional coefficient K_{Lip} of the load converter's inner current loop is the key factor that effects the stability boundary of A_1. The stability boundaries of A_1 under different K_{Lip} values, obtained using traditional methods, improved methods, and simulations are illustrated in Fig. 19. The traditional boundary treats CPLs as ideal, while the improved boundary accounts for actual dynamics. The simulation results confirm that the improved stability boundary aligns more closely with the actual performance, validating the accuracy and effectiveness of this analysis.

REFERENCES

[1] A. Parastar, A. Gandomkar, and J.-K. Seok, "High-efficiency multilevel flying-capacitor DC/DC converter for distributed renewable energy systems," *IEEE Trans. Ind. Electron.*, vol. 62, no. 12, pp. 7620–7630, Dec. 2015.

[2] T. Dragičević, X. Lu, J. C. Vasquez, and J. M. Guerrero, "DC microgrids-Part I: A review of control strategies and stabilization techniques," *IEEE Trans. Power Electron.*, vol. 31, no. 7, pp. 4876–4891, Jul. 2016.

[3] B. He, W. Chen, X. Li, L. Shu, and X. Ruan, "A power adaptive impedance reshaping strategy for cascaded DC system with buck-type constant power load," *IEEE Trans. Power Electron.*, vol. 37, no. 8, pp. 8909–8920, Aug. 2022.

[4] A. Emadi, A. Khaligh, C. Rivetta, and G. Williamson, "Constant power loads and negative impedance instability in automotive systems: Definition, modeling, stability, and control of power electronic converters and motor drives," *IEEE Trans. Veh. Technol.*, vol. 55, no. 4, pp. 1112–1125, Jul. 2006.

[5] A. Kwasinski and C. N. Onwuchekwa, "Dynamic behavior and stabilization of DC microgrids with instantaneous constant-power loads," *IEEE Trans. Power Electron.*, vol. 26, no. 3, pp. 822–834, Mar. 2011.

[6] M. Cespedes, L. Xing, and J. Sun, "Constant-power load system stabilization by passive damping," *IEEE Trans. Power Electron.*, vol. 26, no. 7, pp. 1832–1836, Jul. 2011.

[7] A. Khaligh, "Realization of parasitics in stability of DC-DC converters loaded by constant power loads in advanced multiconverter automotive systems," *IEEE Trans. Ind. Electron.*, vol. 55, no. 6, pp. 2295–2305, Jul. 2008.

[8] A. M. Rahimi and A. Emadi, "An analytical investigation of DC/DC power electronic converters with constant power loads in vehicular power systems," *IEEE Trans. Veh. Technol.*, vol. 58, no. 6, pp. 2689–2702, Jul. 2009.

[9] X. Liu, A. J. Forsyth, and A. M. Cross, "Negative input-resistance compensator for a constant power load," *IEEE Trans. Ind. Electron.*, vol. 54, no. 6, pp. 3188–3196, Dec. 2007.

[10] M. A. Hassan, E.-p. Li, X. Li, T. Li, C. Duan, and S. Chi, "Adaptive passivity-based control of DC-DC buck power converter with constant power load in DC microgrid systems," *IEEE Trans. Emerg. Sel. Topics Power Electron.*, vol. 7, no. 3, pp. 2029–2040, Sep. 2019.

[11] M. Wang, F. Tang, X. Wu, Y. Zhang, and J. Wang, "Passivation and passivity-based control of DC-DC converter with unknown constant power loads," *IEEE Trans. Emerg. Sel. Topics Power Electron.*, vol. 10, no. 4, pp. 4041–4058, Aug. 2022.

[12] M. Abdolahi, J. Adabi, and S. Y. M. Mousavi, "An adaptive extended Kalman filter with passivity-based control for DC-DC converter in DC microgrids supplying constant power loads," *IEEE Trans. Ind. Electron.*, vol. 71, no. 5, pp. 4873–4882, May 2024.

[13] Y. Zhao, W. Qiao, and D. Ha, "A sliding-mode duty-ratio controller for DC/DC buck converters with constant power loads," *IEEE Trans. Ind. Appl.*, vol. 50, no. 2, pp. 1448–1458, Mar./Apr. 2014.

[14] C. Zheng, T. Dragičević, J. Zhang, R. Chen, and F. Blaabjerg, "Composite robust quasi-sliding mode control of DC-DC buck converter with constant power loads," *IEEE Trans. Emerg. Sel. Topics Power Electron.*, vol. 9, no. 2, pp. 1455–1464, Apr. 2021.

[15] J. A. Solsona, S. G. Jorge, and C. A. Busada, "Nonlinear control of a buck converter which feeds a constant power load," *IEEE Trans. Power Electron.*, vol. 30, no. 12, pp. 7193–7201, Dec. 2015.

[16] J. Wu and Y. Lu, "Feedback linearization adaptive control for a buck converter with constant power loads," in *Proc. 2018 IEEE Int. Power Electron. Application Conf. Expo.*, 2018, pp. 1–6.

[17] Q. Xu, C. Zhang, C. Wen, and P. Wang, "A novel composite nonlinear controller for stabilization of constant power load in DC microgrid," *IEEE Trans. Smart Grid*, vol. 10, no. 1, pp. 752–761, Dec. 2019.

[18] N. Sarrafan et al., "A novel fast fixed-time backstepping control of DC microgrids feeding constant power loads," *IEEE Trans. Ind. Electron.*, vol. 70, no. 6, pp. 5917–5926, Jun. 2023.

[19] H. Lin, H. S.-H. Chung, R. Shen, and Y. Xiang, "Enhancing stability of DC cascaded systems with CPLs using MPC combined with ni and accounting for parameter uncertainties," *IEEE Trans. Power Electron.*, vol. 39, no. 5, pp. 5225–5238, May 2024.

[20] Q. Xu, Y. Yan, C. Zhang, T. Dragicevic, and F. Blaabjerg, "An offset-free composite model predictive control strategy for DC/DC buck converter feeding constant power loads," *IEEE Trans. Power Electron.*, vol. 35, no. 5, pp. 5331–5342, May 2020.

[21] W. He and R. Ortega, "Design and implementation of adaptive energy shaping control for DC-DC converters with constant power loads," *IEEE Trans. Ind. Informat.*, vol. 16, no. 8, pp. 5053–5064, Aug. 2020.

[22] C. Zhang, M. Li, L. Zhou, C. Cui, and L. Xu, "A variable self-tuning horizon mechanism for generalized dynamic predictive control on DC/DC boost converters feeding CPLs," *IEEE Trans. Emerg. Sel. Topics Power Electron.*, vol. 11, no. 2, pp. 1650–1660, Apr. 2023.

[23] G. Duan, "High-order fully actuated system approaches: Part i. models and basic procedure," *Int. J. Syst. Sci.*, vol. 52, no. 2, pp. 422–435, 2021.

[24] P. Li and G. Duan, "High-order fully actuated control approaches of flexible servo systems based on singular perturbation theory," *IEEE/ASME Trans. Mechatron.*, vol. 28, no. 6, pp. 3386–3397, Dec. 2023.

[25] G. Duan, "High-order fully actuated system approaches: Part VII. controllability, stabilizability and parametric design," *Int. J. Syst. Sci.*, vol. 52, no. 14, pp. 3091–3114, 2021.

[26] D.-W. Zhang, G.-P. Liu, and L. Cao, "Constrained cooperative control for high-order fully actuated multiagent systems with application to air-bearing spacecraft simulators," *IEEE/ASME Trans. Mechatron.*, vol. 28, no. 3, pp. 1570–1581, Jun. 2023.

[27] S. Lu, K. Tsakalis, and Y. Chen, "Development and application of a novel high-order fully actuated system approach—Part I: 3- DOF quadrotor control," *IEEE Contr. Syst. Lett.*, vol. 7, pp. 1177–1182, 2023.

[28] Y. Yu, G.-P. Liu, Y. Huang, and J. M. Guerrero, "Distributed learning-based secondary control for islanded DC microgrids: A high-order fully actuated system approach," *IEEE Trans. Ind. Electron.*, vol. 71, no. 3, pp. 2990–3000, Mar. 2024.

[29] G. Duan, "High-order fully actuated system approaches: Part III. robust control and high-order backstepping," *Int. J. Syst. Sci.*, vol. 52, no. 5, pp. 952–971, 2021.

[30] A. Emadi and M. Ehsani, "Negative impedance stabilizing controls for PWM DC-DC converters using feedback linearization techniques," in *Proc. Collection Tech. Papers. 35th Intersociety Energy Convers. Eng. Conf. Exhibit*, 2000, vol. 1, pp. 613–620.

[31] R. C. Dorf and R. H. Bishop, *Modern Control Systems*. Upper Saddle River, NJ, USA: Pearson Prentice Hall, 2008.
[32] H. G. Narm, S. Eren, and M. Karimi-Ghartemani, "A robust controller with integrated plant dynamics for constant power loads in DC microgrid," *IEEE Trans. Power Electron.*, vol. 38, no. 4, pp. 4419–4429, Apr. 2023.
[33] Y.-C. Jeung, D.-C. Lee, T. Dragičević, and F. Blaabjerg, "Design of passivity-based damping controller for suppressing power oscillations in DC microgrids," *IEEE Trans. Power Electron.*, vol. 36, no. 4, pp. 4016–4028, Apr. 2021.
[34] W.-H. Chen, "Disturbance observer based control for nonlinear systems," *IEEE/ASME Trans. Mechatron.*, vol. 9, no. 4, pp. 706–710, Dec. 2004.
[35] C. N. Onwuchekwa and A. Kwasinski, "Analysis of boundary control for buck converters with instantaneous constant-power loads," *IEEE Trans. Power Electron.*, vol. 25, no. 8, pp. 2018–2032, Aug. 2010.
[36] J. Jiang et al., "A conservatism-free large signal stability analysis method for DC microgrid based on mixed potential theory," *IEEE Trans. Power Electron.*, vol. 34, no. 11, pp. 11342–11351, Nov. 2019.

Yadong Wei (Student Member, IEEE) was born in Xinjiang, China, in 1997. He received the B.S. degree in electrical engineering and automation, in 2020, from the School of Electric Power, South China University of Technology, Guangzhou, China, where he is currently working toward the Ph.D. degree in electrical engineering.

His current research interests include the circuit topology and control strategy of ad/dc converter, modeling, and nonlinear control of power electronic converters.

Bo Zhang (Fellow, IEEE) was born in Shanghai, China, in 1962. He received the B.S. degree in electrical engineering from Zhejiang University, Hangzhou, China, in 1982, the M.S. degree in power electronics from Southwest Jiaotong University, Chengdu, China, in 1988, and the Ph.D. degree in power electronics from the Nanjing University of Aeronautics and Astronautics, Nanjing, China, in 1994.

He is currently a Professor with the School of Electric Power, South China University of Technology, Guangzhou, China. He has authored or coauthored more than 600 papers and held over 230 patents. He has authored nine monographs. His research interests include nonlinear analysis and control of power electronics, wireless power transfer technology, and ac drives.